Spinodals, scaling, and ergodicity in a threshold model with long-range stress transfer

C. D. Ferguson,[1,*] W. Klein,[1] and John B. Rundle[2]
[1]*Physics Department, Center for Polymer Physics, and Center for Computational Science, Boston University, 590 Commonwealth Avenue, Boston, Massachusetts 02215*
[2]*Department of Geological Sciences and CIRES, University of Colorado, Boulder, Colorado 80309*
(Received 26 October 1998)

We present both theoretical and numerical analyses of a cellular automaton version of a slider-block model or threshold model that includes long-range interactions. Theoretically we develop a coarse-grained description in the mean-field (infinite range) limit and discuss the relevance of the metastable state, limit of stability (spinodal), and nucleation to the phenomenology of the model. We also simulate the model and confirm the relevance of the theory for systems with long- but finite-range interactions. Results of particular interest include the existence of Gutenberg-Richter-like scaling consistent with that found on real earthquake fault systems, the association of large events with nucleation near the spinodal, and the result that such systems can be described, in the mean-field limit, with techniques appropriate to systems in equilibrium.
[S1063-651X(99)02908-6]

PACS number(s): 05.40.−a, 02.60.Cb, 91.30.Px

I. INTRODUCTION

It is well known that the frequency-size statistics of earthquakes obey Gutenberg-Richter (GR) scaling relations [1]. However, it is not known whether critical phenomena produce these empirical relations. To see if this connection exists, geophysicists [2–5] and condensed-matter physicists [6–10] have been examining models of earthquake faults which hopefully contain the minimal, but essential, physics. In the first of these models, Burridge and Knopoff [11] (BK) constructed a one-dimensional network of slider blocks connected to their nearest neighbors and a loader plate via linear elastic springs. The BK model and other models [2–10] influenced by it can exhibit frequency-size statistics similar to GR scaling. However, until recently no theoretical analysis has demonstrated a connection between this scaling and critical phenomena. On the contrary, after analyzing the behavior of a single BK slider block, Vasconcelos [12] argued that a first-order phase transition occurs but that no continuous phase transition, giving rise to critical phenomena, exists. In a previous paper [13], we undertook a theoretical analysis and developed a coarse-grained description of a cellular automaton (CA) long-range interaction version of the BK model based on the work of Rundle, Jackson, and Brown (RJB) [4,5] that indicated the presence of a spinodal critical point, which can give rise to the GR scaling observed in these models. In this paper, we report on more extensive investigations of this CA model. In addition to providing a fuller description of our coarse-grained theory and its assumptions, we also present the results of simulations that are consistent with this theory. In particular, we find critical slowing down as the spinodal critical point is approached, frequency-size statistics for a wide range of realistic fault parameters that are consistent with the values predicted by the theory, and a strong relationship between earthquakes in the model and nucleation events.

In addition, we have investigated further a previous result [14] that the mean-field (infinite range interactions) version of this model can be described by an equilibrium theory. We find that for slow tectonic driving and long-range interactions, the CA model demonstrates what we call local ergodic behavior. We demonstrate this using a measure of effective ergodicity developed by Thirumalai and Mountain [15,16]. This result as well as the theoretical analysis gives further weight to the claim [13,14] that various aspects of this model can be described by the techniques of equilibrium statistical mechanics.

The remainder of this paper is structured as follows. In Sec. II, we briefly describe the RJB version of the BK model. In Sec. III, we discuss the applicability of long-range interactions to models of earthquake faults and develop a coarse-grained theory for the long-range CA model. In Sec. IV, we discuss the assumptions made in the development of this theory and present numerical evidence supporting their validity. In Sec. V we review spinodal nucleation and present the predictions of the theory as well as the corresponding simulation results. In Sec. VI, we apply a measure of effective ergodicity, the energy-fluctuation metric, to the CA model and find that the system tends toward ergodic behavior as the tectonic velocity approaches zero and as the interaction range increases. In Sec. VII, we discuss the arresting of nucleation events and return to the question of coarse graining. Finally, in Sec. VIII, we discuss our results.

II. MODEL

In this section we describe the model introduced by Rundle, Jackson, and Brown. This model consists of a two-dimensional array of massless blocks that interact with their neighbors and a tectonic loader plate via linear springs with constants K_C and K_L, respectively. Initially, each block i receives a random position U_i from a uniform distribution. The loader plate contribution to the stress is set equal to zero initially, and the stress σ_i on each block is measured and compared to a threshold value σ_i^F. If $\sigma_i < \sigma_i^F$, then the block is not moved. If, however, $\sigma_i \geqslant \sigma_i^F$, the block is moved according to the rule

*Present address: Federation of American Scientists, Washington, DC 20002.

$$U_i(t+1)=U_i(t)+\left[\frac{\sigma_i(t)-\sigma_i^R}{K}\right][1-\eta_i(t)]\Theta(\sigma_i(t)-\sigma_i^F). \tag{2.1}$$

Here the step function $\Theta(x)=0 \ \forall x\leqslant 0$ and $=1 \ \forall x>0$, and the effective spring constant $K=K_L+\Sigma_{j,i\neq j}T_{ij}$, where T_{ij} is a matrix of interaction coefficients. The sum over j includes all of the neighbors of block i. The residual stress σ_i^R is a parameter that specifies the stress on a block immediately after failure. All blocks are tested and moved until no block has a stress greater than σ_i^F. At this point the plate is moved. Two procedures are used. The first, which we will refer to as the zero velocity limit, requires that we find the block that has the highest σ_i. We then move the plate so that each block receives the stress that just brings the block with the highest stress to its failure threshold. This guarantees that in the vast majority of plate updates there will be only one initial failure site and hence one earthquake per plate update. The second method we will employ is to move the plate a fixed distance $V\Delta T$, thereby increasing the stress σ_i on each block i by $K_L V\Delta T$. The quantity ΔT determines the ''tectonic'' time scale, which is taken to be $\Delta T=1$ for the moment. We will return to the question of this time scale in Sec. VII. After the plate is moved, the stress on each block is calculated via

$$\sigma_i(t)=\sum_j T_{ij}U_j(t)+K_L V\sum_n \Theta(n-t), \tag{2.2}$$

and the process outlined above is repeated.

The step function mathematically expresses the Mohr-Coulomb friction law, which has the useful property that it is always scale invariant [17]. In this paper, we use the stochastic CA model [14], in which $\eta_i(t)$ is a random noise equal to ρW, where ρ is a uniformly distributed random number $\in[0,1]$ and the predetermined noise amplitude W is in the range $0\leqslant W\leqslant 1$.

After block i slips, each neighbor of the failed block receives the amount of stress $K_C[\sigma_i(t)-\sigma_i^R]/K$, while the system dissipates the amount $K_L[\sigma_i(t)-\sigma_i^R]/K$. This stress transfer may cause these neighbors to slip and so on, thus initiating an earthquake, or avalanche, which continues until every block has $\sigma_j<\sigma_j^F$. The size of an earthquake equals the number of slipped blocks after each plate update. We count each slip as a block failure even if a block slips more than once. In most cases of interest in this work, multiple slips of a block during one event are rare. The count begins anew after each update of the loader plate. It is the properties of the earthquakes or avalanches in this model that we have studied theoretically and via simulations.

III. LONG-RANGE INTERACTIONS AND COARSE GRAINING OF MODEL

In this work we will concentrate on the long-range interaction version of the CA model. We do so for the following reasons. Linear elasticity theory yields long-range stress tensors for a variety of geophysical applications [18], including idealized viscoelastic faults. For a two-dimensional dislocation in a three-dimensional homogeneous elastic medium, the magnitude T of the static stress tensor goes as $T\sim 1/r^3$ [19]. While geophysicists do not know the actual stress tensors for real faults, they expect that long-range stress tensors, which are similar to the $1/r^3$ interaction, apply to faults. It is suspected that microcracks in a fault, as well as other ''defects'' such as water, screen the $1/r^3$ interaction, leading to a proposed $e^{-\alpha r}/r^3$ interaction, where $\alpha\ll 1$, implying a slow decay to the long-range interaction over the fault's extent [20].

In addition, a fault's interaction strength varies with and extends over a fault's depth, which is on the order of a kilometer or more. Because our CA slider block models a macroscopic fault asperity, which has a linear dimension on the order of ten meters, the interaction range should span on the order of one hundred blocks in length. To approximately account for the screening and depth effects, we can truncate the $1/r^3$ interaction or any appropriate long-range interaction.

In addition, recent observations [21,22] of seismic activity following some large magnitude ($\gtrsim 7$ on the Richter scale) events indicate long-range correlations of subsequent activity with the main quake, occurring within a few minutes after and extending up to 1200 km (much further than the typical aftershock zone) from the main shock. Hill *et al.* [21] proposed models with long-range stress tensors, including $1/r^3$, to explain these spatial correlations.

In nature, the average earthquake stress drop $\Delta\sigma$ is approximately 0.01–1 MPa, which is small compared to the failure threshold ($\sigma^F\approx 10$ MPa) or the breaking strength of rock [23]. Consequently, the ratio $\Delta\sigma/\sigma^F\approx 0.001-0.1$. For a fixed σ^F in the long-range CA model, $\Delta\sigma$ decreases as the interaction range increases because the mean interaction strength or interblock spring constant decreases as the interaction range increases [24]. To obtain a consistent ratio $\Delta\sigma/\sigma^F$ with geological faults, the CA model's interaction region must include several hundred blocks.

Finally, in addition to questions of interest in earthquake physics, we want to investigate mean-field effects in driven dissipative systems which appear as the CA model becomes more long-range. In particular, our coarse-grained theory (developed below) indicates that a spinodal critical point influences earthquake scaling, the structure of an earthquake, and the amount of time required to form an earthquake during a tectonic plate update. In addition, earlier simulations [14] and theoretical analysis [13] indicate that these systems are locally ergodic in the limit of infinite interaction range. The concept of local ergodicity will be addressed in Sec. VI. We know that long-range systems [25–27,14] can display different physics than short-range systems. This model, due to the fact that it is driven and dissipative, is a particularly interesting one on which to study this phenomenon. We begin with the theoretical analysis.

In Ref. [13], we derived a coarse-grained theory for the CA model. In this paper, we present a more detailed description of this theory. We begin by rewriting Eqs. (2.2) and (2.1) to eliminate the position variable $U_j(t)$ and to develop a stress evolution equation. Multiply Eq. (2.1) by T_{ij}, sum over j, and use Eq. (2.2) to obtain

$$\sigma_i(t+1)-\sigma_i(t)=\frac{1}{K}\sum_j T_{ij}[\sigma_j(t)-\sigma_j^R]\Theta[\sigma_j(t)-\sigma_j^F] + \eta_j'(t)+K_L V, \tag{3.1}$$

where the noise $\eta_j'(t)=\Sigma_j T_{ij}[\sigma_j(t)-\sigma_j^F]\eta_j(t)$ remains spatially random as long as T_{ij} is a radially symmetric interaction, which it is assumed to be. Equation (3.1) gives the new stress on block i at time $t+1$ in terms of the previous stresses from block i, the neighboring j blocks, the loader plate, and the noise. We have assumed that blocks fail only once per plate update, which will be discussed later in this section and in Sec. IV.

The $K_L V$ term was obtained by assuming that the stress loading at time $t+1$ in Eq. (2.2), i.e.,

$$K_L V\sum_n \Theta(n-t-1), \tag{3.2}$$

minus the stress loading at time t was simply the difference between the two sums at $t+1$ and t. This point will require a much more careful discussion, and we will return to it in Sec. VII.

For long-range interactions, the number of neighbors $q \gg 1$. Each block at lattice site i interacts via springs with all blocks at lattice sites j contained within a square interaction region with area $(2R+1)^2$ so that $q=(2R+1)^2-1$. We consider two stress Green's functions: (i) $T_{ij}\sim K_C/|\vec{i}-\vec{j}|^3$, which is truncated at an interaction range R (an infrared cutoff), where $|\vec{i}-\vec{j}|$ is the lattice distance between cells i and j, (ii) $T_{ij}=0$ for $|i-j|>R$, where i and j in $|i-j|$ are the x and y components of $\vec{i}$ and $\vec{j}$, and $T_{ij}=K_C/q$ for $|i-j|\leqslant R$ and $=0$ otherwise. Note that these Green's functions are similar in that both weaken the nearest-neighbor interaction K_C. We also assume a short-range (ultraviolet) cutoff in T_{ij}, which arises due to the natural short-range cutoff of geological and condensed matter systems, so that $T_{ij}\leqslant A<\infty \ \forall i$ and j. The limit $q\to\infty$ produces mean-field behavior, which is qualitatively different from the nearest-neighbor $q=4$ model. For both choices of the Green's function the interaction range scales with q as $R\sim q^{1/2}$.

The only physics of interest in our CA model is on length scales greater than R. By developing a coarse-grained description [28] of Eq. (3.1), with a coarse-graining size of R^2, we can sum over fluctuations on length scales smaller than R and retain the physics at larger length scales. We proceed, therefore, from a microscopic description of the stresses on the individual blocks to a macroscopic description of the stresses on a coarse-grained block in which the stresses become continuous classical variables or fields. In the remainder of this paper, we will assume that σ_i^F and σ_i^R are spatial constants σ^F and σ^R.

To accomplish the coarse graining, we define a coarse-grained cell with a volume q centered at block i and specify a coarse-grained time τ, and we average the stress over both the coarse-grained volume and time. Therefore, $\sigma_i(t)$ becomes $\overline{\sigma}_i(\tau)$ on the left-hand side of Eq. (3.1), where the bar denotes coarse-grained average.

On the right-hand side of Eq. (3.1), we convert the summation over the individual j blocks covering a large region into a summation between interacting coarse-grained blocks restricted to local interactions. Because the first term in Eq. (3.1) is written as a discrete convolution, we can use Fourier-transform techniques to convert Eq. (3.1) into a coarse-grained form. First, expand the Fourier transform of T_{ij} in a power series using the transform variable $|\vec{k}|=k$. Note that with the short- and long-distance cutoffs, we have a bounded function on a finite support and hence are assured that the power series in k exists. Second, we truncate the power series at k^2 in order to express the stress tensor as a local interaction between coarse-grained blocks and invert the Fourier transform to obtain for the first term in Eq. (3.1),

$$\begin{aligned}\sum_j T_{ij}[\sigma_j(t)-\sigma^R]\Theta[\sigma_j(t)-\sigma^F] \\ \sim -qK_C\sum_j \Delta_{ij}[\sigma_j(t)-\sigma^R]\Theta[\sigma_j(t)-\sigma^F] \\ -K_L[\sigma_i(t)-\sigma^R]\Theta[\sigma_i(t)-\sigma^F],\end{aligned} \tag{3.3}$$

where $-K_L$ and qK_C are the zeroth and second moments of T_{ij}, respectively, Δ_{ij} is the matrix (discrete) representation of the Laplacian, and the sum preceding the Laplacian is over the coarse-grained blocks with a length scale set by the coarse-graining scale $q^{1/2}$.

Next, we convert the discrete summation in Eq. (3.3) into a continuous integral. This step transforms σ_j into a continuous variable. To carry out this step, notice that the step function in Eq. (3.3) specifies that only blocks whose stress equals or exceeds σ^F will fail in a coarse-grained time interval τ and thus contribute to the summation. Consequently, we can compute the partial sum of only those blocks that fail within τ.

Before we compute the partial sum, we consider what happens to the time-averaged stress on a block due to the interblock K_C springs in the mean-field limit. From symmetry, this stress becomes very small as $q\to\infty$. We also numerically verified this condition by measuring the mean stress on the blocks and comparing it to the mean stress solely due to the loader plate. Recall that the loader plate stress equals K_L times the mean distance between the actual positions of the blocks and the positions where the loader plate exerts zero force on the blocks. Within a coarse-graining time as q increases, the mean stress on the blocks approaches the mean loader plate stress on the blocks. Using standard mean-field arguments [27], it is expected that the stress fluctuations away from the mean value approach zero as $q^{-1/2}$.

The above discussion implies that the blocks are weakly interacting with each other in the mean-field limit. Thus, from the central limit theorem, within a coarse-grained volume on a time scale shorter than the coarse-grained time τ, the blocks' stress distribution will equilibrate to a Gaussian centered about $\overline{\sigma}(\vec{x},\tau)$, where $\vec{x}$ labels the coarse-grained volume. In the next section, we discuss the numerical evidence that the stress distribution equilibrates to a Gaussian on time scales less than τ.

Also, within the coarse-grained time, only blocks with stress lying between σ_0 and σ^F will fail, where $0<\sigma_0<\sigma^F$, because the loader plate will add only enough stress to bring blocks with stress σ_0 or greater to failure. Here σ_0 is a parameter to be determined later. The above considerations lead to the following Gaussian representation of the partial sum:

$$\frac{1}{q}\sum_j{}' [\sigma_j(t)-\sigma^R]\Theta[\sigma_j(t)-\sigma^F]$$
$$=(\sigma^F-\sigma^R)\sqrt{\beta/\pi}\int_{\sigma_0}^{\sigma^F} d\sigma \exp\{-\beta[\sigma-\overline{\sigma}(\vec{x},\tau)]^2\}, \tag{3.4}$$

where the prime on the summation means that the sum includes only the blocks that fail inside the coarse-grained volume in a coarse-grained time. The factor $\sigma^F-\sigma^R$ arises from the fact that if all q blocks failed, then the left-hand side of Eq. (3.4) is exactly $\sigma^F-\sigma^R$ in the $\beta\to\infty$ limit.

In developing this Gaussian approximation, we assume that a block fails at most once during a coarse-grain time τ. These assumptions are correct in the $q\to\infty$ limit for $V<V_c=(\sigma^F-\sigma^R)/K$, as demonstrated in the next section. The velocity V_c is a good approximation to the spinodal value for the ranges of β we investigate in this work. Beyond this value of the velocity, the low stress phase is unstable. A detailed discussion of this last point will be presented in a future publication [29]. In this work we will restrict ourselves to a discussion of the low stress phase. However, we will return to this point in Sec. VII. In Eq. (3.4), β specifies the level of noise in the system and plays the role of an inverse temperature so that $\beta\gg 1$ implies low noise compared to $\beta\ll 1$ for high noise. The quantity β also determines the width of the Gaussian and the weight assigned to the ''entropy'' term, developed below. Because of β's dual roles, we assume that the Gaussian and ''entropy'' terms have the same noise dependence [30]. The quantity $\sqrt{\beta/\pi}$ approximates the normalization for $\beta\gg 1$, which follows because a large β produces a narrow Gaussian distribution and allows σ^F to be replaced by infinity in the upper integration limit, causing negligible error in the normalization. In this work we always assume $\beta\gg 1$ since small amplitude noise is what is expected on earthquake faults.

Finally, we derive an ''entropy'' term that counts the number of ways $N(\overline{\sigma}(\vec{x},\tau))$ to distribute the available stress $q\overline{\sigma}(\vec{x},\tau)$ among the q blocks within a coarse-grained volume, where the stress values range from σ^R to σ^F. Over the coarse-graining time, the stress inside a coarse-grained volume will tend to cluster around the mean value of this stress range, i.e., $\overline{\sigma}=(\sigma^F+\sigma^R)/2$. The entropy equals minus the logarithm of the distribution $N(\overline{\sigma}(\vec{x},\tau))$. For nonequilibrium thermodynamical systems near equilibrium, where the long-range CA model is such a system [14], the system's entropy can be expressed as the potential of a generalized force (see, e.g., Ref. [31]), which gives the following term:

$$\frac{\delta S(\overline{\sigma}(\vec{x},\tau))}{\delta\overline{\sigma}(\vec{x},\tau)}=-\frac{\delta \ln N(\overline{\sigma}(\vec{x},\tau))}{\delta\overline{\sigma}(\vec{x},\tau)}=\frac{\beta^{-1}}{\sigma^F-\sigma^R}\ln\left[\frac{\overline{\sigma}(\vec{x},\tau)-\sigma^R}{\sigma^F-\overline{\sigma}(\vec{x},\tau)}\right]$$
$$-\frac{\beta^{-1}}{\sigma^F-\sigma^R}\int_{\sigma^R}^{\sigma^F} d\sigma \ln\left[\frac{\sigma-\sigma^R}{\sigma^F-\sigma}\right]$$
$$\times\exp\{-\beta[\sigma-\overline{\sigma}(\vec{x},\tau)]^2\} \tag{3.5}$$

for the $\overline{\sigma}(\vec{x},\tau)$ equation of motion.

To obtain the coarse-grained equation of motion, we combine Eqs. (3.1), (3.3), (3.4), and (3.5), take the temporal and spatial continuum limits, and obtain

$$\frac{\partial\overline{\sigma}(\vec{x},\tau)}{\partial\tau}=K_L V+\overline{\eta}(\vec{x},\tau)+\frac{[qK_C\nabla^2-K_L]}{K}\frac{(\sigma^F-\sigma^R)}{2}$$
$$\times\{\mathrm{erf}-\sqrt{\beta}[\sigma^F-\overline{\sigma}(\vec{x},\tau)]\}$$
$$-\mathrm{erf}\{\sqrt{\beta}[\sigma_0-\overline{\sigma}(\vec{x},\tau)]\}-\frac{\beta^{-1}}{\sigma^F-\sigma^R}$$
$$\times\left(\ln\left[\frac{\overline{\sigma}(\vec{x},\tau)-\sigma^R}{\sigma^F-\overline{\sigma}(\vec{x},\tau)}\right]-\left[\frac{\beta}{\pi}\right]^2\int_{\sigma^R}^{\sigma^F} d\sigma \ln\left[\frac{\sigma-\sigma^R}{\sigma^F-\sigma}\right]\right.$$
$$\left.\times\exp\{-\beta[\sigma-\overline{\sigma}(\vec{x},\tau)]^2\}\right), \tag{3.6}$$

where erf(z) is the error function, which came from the Gaussian in Eq. (3.4), and $\overline{\eta}(\vec{x},\tau)$ is the coarse-grained noise. We can obtain the equation for the time-independent spatially homogeneous solutions to Eq. (3.6) by setting the noise and the derivatives to zero to obtain

$$K_L V=\frac{K_L}{K}\frac{(\sigma^F-\sigma^R)}{2}$$
$$\times\{\mathrm{erf}[\sqrt{\beta}(\sigma^F-\overline{\sigma})]-\mathrm{erf}[\sqrt{\beta}(\sigma_0-\overline{\sigma})]\}$$
$$+\frac{\beta^{-1}}{\sigma^F-\sigma^R}\left(\ln\left[\frac{\overline{\sigma}-\sigma^R}{\sigma^F-\overline{\sigma}}\right]-\left[\frac{\beta}{\pi}\right]^{1/2}\right.$$
$$\left.\times\int_{\sigma^R}^{\sigma^F} d\sigma \ln\left[\frac{\sigma-\sigma^R}{\sigma^F-\sigma}\right]\exp[-\beta(\sigma-\overline{\sigma})^2]\right). \tag{3.7}$$

The right-hand side of Eq. (3.7) represents the rate of stress dissipation over the coarse-grained time and system volume, and the left-hand side of Eq. (3.7) equals the rate of stress input into the system.

The initial conditions specify all the parameters except σ_0. We can determine σ_0 by considering the $q\to\infty$ limit in which blocks within the interaction range are essentially noninteracting. This noninteracting effect occurs because if every block interacts with all other blocks, there can be no spatial scale for fluctuations so that the interactions can be combined into an effective or mean field. By assuming that every block interacts with all other blocks, we can still calculate mean-field thermodynamics [28], and we have that the spatial and temporal average of $\overline{\sigma}(\vec{x},\tau)$ must be $\overline{\sigma}=(\sigma^F+\sigma^R)/2$. Substituting $\overline{\sigma}$ into Eq. (3.7) and noting that the ''entropy'' term equals zero for this $\overline{\sigma}$, we get the following equation:

$$\frac{\sigma^F-\sigma^R}{2K}\left\{\mathrm{erf}\left[\sqrt{\beta}\frac{\sigma^F-\sigma^R}{2}\right]-\mathrm{erf}\left[\sqrt{\beta}\left(\sigma_0-\frac{\sigma^F+\sigma^R}{2}\right)\right]\right\}=V, \tag{3.8}$$

which we can solve for σ_0.

Now that we have derived the coarse-grained equation, we can obtain the physics of the CA model after specifying the four parameters β, K/K_L, VK_L, and $(\sigma^F-\sigma^R)/K$, which determine the behavior of the equation and the model. Using the values of these parameters representative of those for real earthquake faults, such that $\Delta\sigma/\sigma^F\approx 0.001-0.1$ and

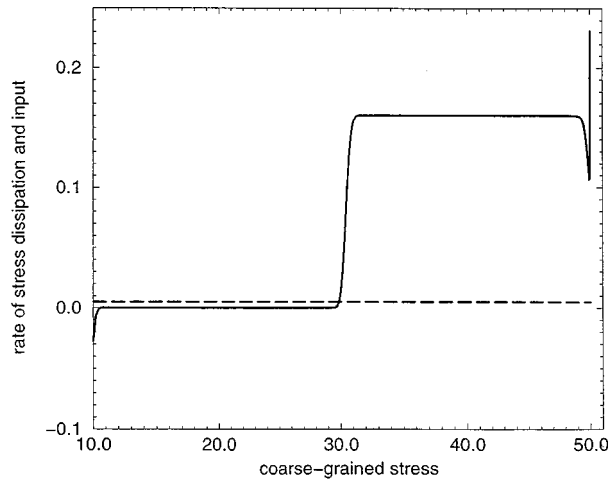

FIG. 1. Solution to the time-independent spatially homogeneous Eq. (3.7), using parameters $K=100$, $\sigma^F=50$, $\sigma^R=10$, $\beta=5$, and $V=0.005$. The solid line represents the rate of stress dissipation from the right-hand side of Eq. (3.7), and the dashed line represents the rate of stress input from the left-hand side of Eq. (3.7).

$V\sim 0$, we numerically solve the time-independent spatially homogeneous equation (3.7) to illustrate some important aspects of the theory. As noted in Sec. II, a typical CA slider block dissipates an amount of stress $\Delta\sigma=(K_L/K)(\sigma^F-\sigma^R)$. We choose values of K_L, K, σ^F, and σ^R that give $\Delta\sigma/\sigma^F$ values consistent with real faults. In Fig. 1, $K_L=1$, $K=100$, $\sigma^F=50$, and $\sigma^R=10$ so that $\Delta\sigma/\sigma^F=8\times10^{-3}$, and in Fig. 2 we increase K to 1000 so that $\Delta\sigma/\sigma^F=8\times10^{-4}$. For both figures, we use $\beta=5$, assuming that noise does not strongly influence the fault, and we set $V=0.005$ to slowly drive the system. To obtain these curves, we also need to compute σ_0, which we numerically calculated from Eq. (3.8). In Figs. 1 and 2, the solid curve comes from the right-hand side of Eq. (3.7) and equal the mean rate of stress dissipation, while the dashed straight line comes from the left-hand side of Eq. (3.7) and equals the mean rate of stress input. Therefore, the intersection of the two curves determines the spatially and temporally averaged stress $\overline{\sigma}$ at which the rates of stress dissipation and input balance each other.

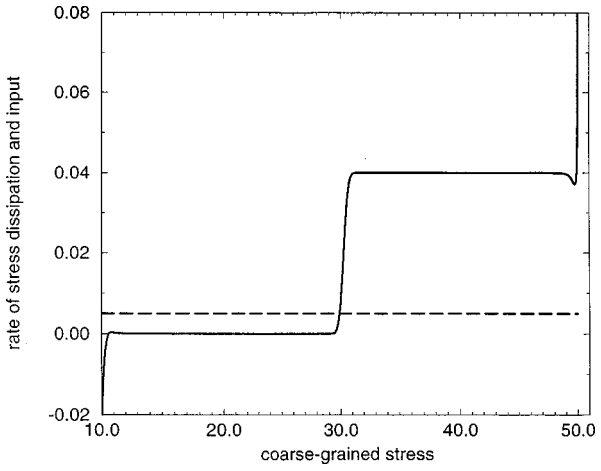

FIG. 2. Solution to the time-independent spatially homogeneous Eq. (3.7), using the same parameters as Fig. 1, except $K=1000$. The solid line represents the rate of stress dissipation from the right-hand side of Eq. (3.7), and the dashed line represents the rate of stress input from the left-hand side of Eq. (3.7).

Analyzing the solutions of Eq. (3.6), we make the following observations. In Figs. 1 and 2, the intersection of the horizontal line representing the mean velocity V and the curve representing the right-hand side of Eq. (3.6) occurs in the low stress regime. In simulations of the CA model with approximately the same parameters, $\overline{\sigma}$ is approximately equal to the values in these figures obtained from the coarse-grained equation (3.8) Because the steady-state solutions in Figs. 1 and 2 come from a mean-field theory, we do not expect these solutions to agree exactly with the simulations, which are limited to finite, but long-range, interactions. What happens if either $\Delta\sigma$ is decreased or V or is increased, or both? The curves would then intersect at two additional positive values near $\overline{\sigma}=50$. Although both of these intersection points belong to high stress regimes, the left intersection (lower stress) is unstable, and the right one (higher stress) is metastable. In stress space, a very small distance separates these metastable and unstable states. Observe also in the figures that the well depth decreases as K increases, thus decreasing the range of driving velocities over which the system can explore the higher stress states. For even higher values of V, the high stress phase is stable while the low stress phase is metastable. If V is set higher still, the low stress phase ceases to exist.

Even though the top of the rate of stress dissipation curve appears flat, it is slightly curved with a curvature that depends on β. For smaller β, the top becomes more curved. In contrast, for larger β, the curve steepens and approaches a step function, and the well becomes deeper and tends toward the half-way point between the top and bottom of the curve. As discussed in Ref. [13], the top of the curve and the bottom of the well delineate spinodal critical points, which separate metastable and unstable states. By increasing K, we can bring the spinodal critical points closer to the rate of stress input line. Consequently, as the intersection point nears the spinodal critical points, the system is more likely to experience critical behavior such as scaling induced by th the spinodal. In Sec. V, we present simulation results that demonstrate the effects of the spinodal.

IV. COARSE-GRAINING ASSUMPTIONS

In this section, we present simulation results relevant to clarifying the coarse-graining assumptions used in the preceding section. The three assumptions we examine are as follows. (i) The number of times a block fails per coarse graining time is one. (ii) The stress at which the blocks fail is σ^F and not greater. (iii) The time-averaged stress distribution within a coarse-grained volume is a Gaussian. These assumptions are all made in the mean-field ($q\rightarrow\infty$) limit.

The assumption that a block should fail no more than once during a plate update as $q\rightarrow\infty$ for $V<(\sigma^F-\sigma^R)/K$ (the spinodal velocity) is tested in Fig. 3. We show a log-log plot of the number of multiple failures normalized by the total number of failures. Since the value of K used in the simulations is large, we test the assumption for $V\sim 0$ to satisfy $V<V_c$. The data show that this ratio decreases as q^{-2}. Consequently, the simulation results validate the assumption that

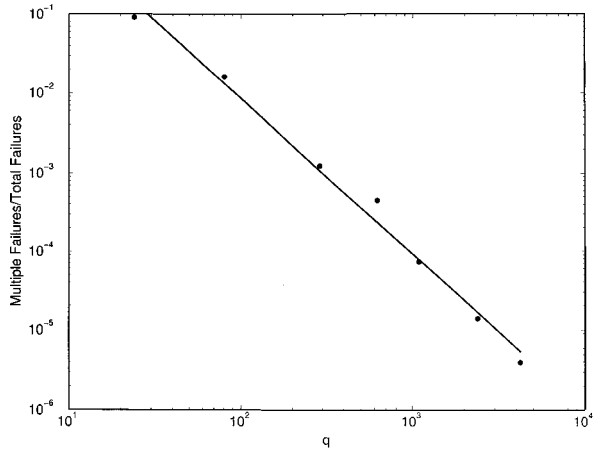

FIG. 3. The number of multiple failures normalized by the total number of failures versus q, where the number of plate updates $n = 35\,000$, using parameters $K_L = 1$, $K_C = 200$, $\sigma^F = 50$, $V \sim 0$, 256×256 system size, $W = 0.3$, and the K_C/q interaction.

the multiple failures can be ignored as q becomes large.

We also assumed that a block's stress before failure does not exceed σ^F in the $q \to \infty$ limit for $V < (\sigma^F - \sigma^R)/K$. Figure 4 shows that as q becomes large, the time-averaged value of the failure stress that exceeds σ^F decreases almost linearly with q. Thus, the simulations again validate the assumption. Note that for the first two assumptions tested with data shown in Figs. 3 and 4, we used a very large value of $K_C = 200$. Because this value typically produces a great number of multiple failures and high values of failure stress relative to σ^F for small q, these data signify a stringent test of the assumptions.

Next we present evidence that the stress within a coarse-grained volume becomes Gaussian distributed within a short time scale compared to the time required for all the blocks within that volume to fail. Figure 5 shows binned temporally averaged stress within a coarse-grained volume of size 256×256. The sequence of plots depicts the evolution of this time-averaged stress from $\approx$20% to 100% of the blocks failing (the caption shows the exact percentages). Before computing the temporal average of each block's stress, the blocks failed several times each to allow the system to move

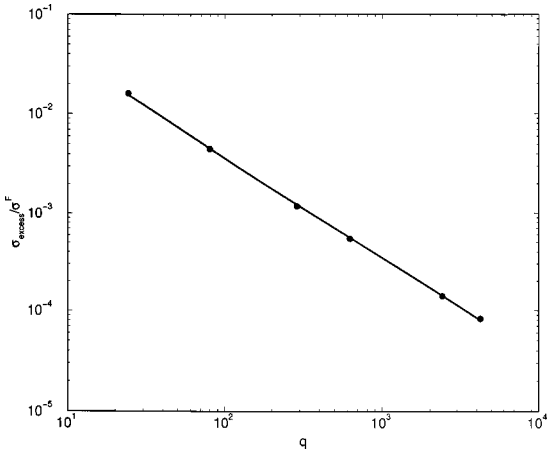

FIG. 4. Time-averaged excess stress normalized by σ^F versus q, using the same system parameters as Fig. 3.

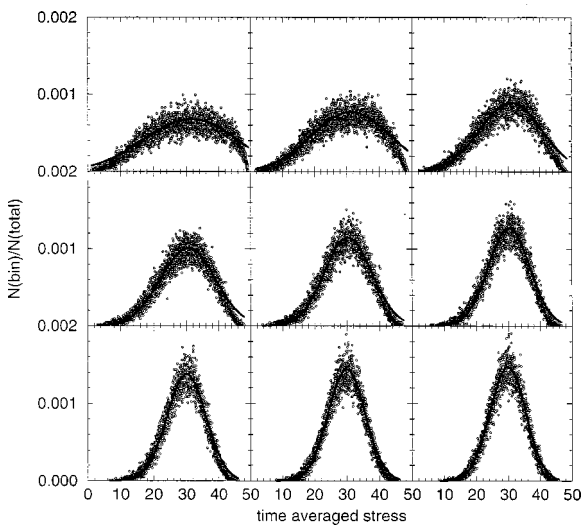

FIG. 5. Histograms of the time-averaged stress in a coarse-grained volume containing 256×256 blocks with bin size equal to 0.02 in units of stress, showing the temporal evolution of the stress in the system, where the earliest to latest times go from left to right and top to bottom. These plots correspond to an increasing number of cumulative failures in terms of the percentage of the total number of blocks that have failed, where the percentages are 20.4, 33.0, 43.2, 55.5, 65.3, 76.8, 86.3, 95.6, and 105.8. The data were collected only after each block had failed several times. The binned simulation data are represented by circles, while the solid curve is a Gaussian fit to the data. The other system parameters are $\sigma^F = 50$, $K_L = 1$, $V \sim 0$, $W = 0.3$, and $K_C = 1$.

away from the transient state due to the initial conditions. Notice that after about $\approx$20% failures, the stress distribution clearly deviates from a flat distribution, which is the distribution after a single plate update. After $\approx$40% failures, the stress distribution appears Gaussian distributed, and it becomes more so as more failures occur. The solid curves in Fig. 5 come from Gaussian fits to the data, where the results are listed in Table I. To compute these fits, we used the Levenberg-Marquardt method of nonlinear fitting [32]. In Table I, observe that the amplitude A increases while the mean $\overline{x}$ and the standard deviation σ decrease as the stress distributions evolve. The σ and $\tilde{\chi}^2$ decrease means that the fits are becoming narrower and closer to a Gaussian distribution. The mean $\overline{x}$ approaches the value predicted by the steady-state solution to the mean-field theory. These fits show that the stress distribution equilibrates to a Gaussian on a time scale shorter than the time required for all blocks to fail.

V. THEORETICAL PREDICTIONS AND SIMULATION RESULTS

In this section, we develop scaling relations relevant to the long-range CA model and present simulation results that are consistent with these relations. Our basic premise is that the scaling relations that are seen in the model are caused by the spinodal critical point. However, unlike most attempts to associate the scaling of the earthquake events in slider block or avalanche models with critical fluctuations [7–9], we associate the large earthquake events with arrested spinodal nucleation droplets and the small events with critical phe-

TABLE I. Gaussian fit parameters corresponding to the curves in Fig. 5, where the fitting form is $y = A \exp\{-[(x-\bar{x})/\sigma]^2\}$. The two leftmost columns contain the percentage of the number of failed blocks compared to the total number of blocks in the coarse-grained volume and the cumulative number of failures that determined the ''% failure'' column. The rightmost column lists the reduced χ^2 of the fit.

% failure	Slips	$A(\times 10^{-3})$	$\bar{x}$	σ	$\tilde{\chi}^2(\times 10^{-5})$
20.4	13,349	0.678±0.007	31.526±0.233	20.455±0.479	2.747
33.0	21,624	0.768±0.007	31.271±0.171	17.181±0.334	2.712
43.2	28,281	0.894±0.008	30.909±0.118	13.826±0.215	2.295
55.5	36,357	1.014±0.008	30.573±0.089	11.867±0.160	2.116
65.3	42,795	1.147±0.008	30.373±0.069	10.313±0.121	2.163
76.8	50,355	1.272±0.008	30.225±0.055	9.210±0.097	2.013
86.3	56,557	1.375±0.008	30.063±0.047	8.485±0.083	1.788
95.6	62,673	1.440±0.008	29.911±0.043	8.094±0.075	1.529
105.8	69,365	1.473±0.008	29.826±0.041	7.920±0.072	1.377

nomena fluctuations. We will return to this point at the end of this section. In order to explain our point, we will briefly review the spinodal nucleation idea and explain the concept of arrested nucleation, which we will return to in Sec. VII.

Spinodal nucleation is concerned with nucleation near the spinodal critical point in systems with long-range (but not infinite) interactions [33]. The reason that long range is essential is that spinodal effects are not seen in models with short-range interactions, as will be seen below. However, as a practical matter, in models with long-range interactions, such as the CA model we are considering, spinodal nucleation is the dominant event. The classical events will be strongly suppressed, as we will see below [34].

We begin our discussion of spinodal nucleation with the partition function. This would be the functional integral of the right-hand side of Eq. (3.6). To simplify the discussion, we will use a simple ''ϕ^4'' theory. Since we are only interested in the scaling dependence of various physical quantities, this model will suffice. The partition function z is

$$z = \int \delta\phi \exp\left[-\beta \int d\vec{x} \left(\frac{R^2}{2} (\nabla \phi(\vec{x}))^2 + \epsilon \phi^2(\vec{x}) + \phi^4(\vec{x}) - h\phi(\vec{x}) \right) \right]. \tag{5.1}$$

Here ϵ is $T - T_c$, T_c is the critical temperature, and h can be thought of as an applied magnetic field or a chemical potential. We can scale all lengths with the interaction range R and in the $R \gg 1$ limit obtain the free energy per unit volume, f, from a saddle-point evaluation of Eq. (5.1). Using the relation [35]

$$\frac{\partial \phi(\vec{x},t)}{\partial t} = -M \frac{\delta f(\phi)}{\delta \phi}, \tag{5.2}$$

we define the Langevin dynamics for this system. Here M is a mobility which we will take to be a constant and we now assume a time dependence for $\phi(\vec{x},t)$ given by the Langevin equation (5.2). One could add a noise to the right-hand side of Eq. (5.2), but it will be irrelevant for our considerations. From Eqs. (5.1) and (5.2), and scaling all lengths with R, we obtain

$$\frac{\partial \phi(\vec{x},t)}{\partial t} = -MR^d[-\nabla^2 \phi(\vec{x},t) - 2|\epsilon| \phi(\vec{x},t) + 4\phi^3(\vec{x},t) - h], \tag{5.3}$$

where we have taken $T < T_c$. The equilibrium values of the order parameter $\phi(\vec{x},t)$ can be obtained from Eq. (5.3) by setting all derivatives equal to zero and assuming a solution that is a temporal and spatial constant. The free energy per unit volume f is then

$$f = -|\epsilon| \phi^2 + \phi^4 - h\phi. \tag{5.4}$$

The minima of the free energy corresponding to phases are then the solutions to

$$-2|\epsilon| \phi + 4\phi^3 - h = 0. \tag{5.5}$$

As is easily seen for $\epsilon < 0$, there are two minima. For $h > 0$, the $\phi > 0$ minimum has a lower free energy per unit volume f than the one with $\phi < 0$ and represents the stable phase. The minimum with negative value of ϕ represents the metastable phase and has a higher value of the free energy. As h is increased, the metastable minimum becomes shallower, and finally at $h = h_s$ the metastable minimum disappears. This value of h is referred to as the spinodal value of the field and $\phi = \phi_s$, the value of the metastable minimum when $h = h_s$, is the spinodal value of the order parameter ϕ. We are interested in the mechanism of nucleation out of the metastable well for $\Delta h = h - h_s \ll 1$, $R \gg 1$, $\epsilon < 0$ and fixed, and hence $\phi \sim \phi_s$. This problem has been addressed both theoretically [34,36,37] and via simulations [25,38–40].

The initial step in the theoretical treatment is to find the spinodal values of ϕ and h (ϕ_s and h_s). These values mark the place where the metastable well vanishes. Hence, ϕ_s and h_s must be solutions of Eq. (5.5), and

$$-2|\epsilon| + 12\phi^2 = 0, \tag{5.6}$$

since ϕ_s is an inflection point. We now define a new field $\psi(\vec{x},t) = \phi(\vec{x},t) - \phi_s$ and rewrite Eq. (5.3),

$$\frac{\partial\psi(\vec{x},t)}{\partial t} = -MR^d\Big[-\nabla^2\psi(\vec{x},t) - 12\left(\frac{|\epsilon|}{6}\right)^{1/2}\psi^2(\vec{x},t) + 4\psi^3(\vec{x},t) + \Delta h\Big], \tag{5.7}$$

where we have used Eqs. (5.5) and (5.6) and the fact that ϕ_s is a solution of Eq. (5.5) when $h=h_s$. We now assume, and will demonstrate below, that $\psi(\vec{x},t)\ll 1$ so that we can ignore $\psi^3(\vec{x},t)$ relative to $\psi^2(\vec{x},t)$. We stress that $|\epsilon|>0$ and does not approach zero. It is Δh that approaches zero as we approach the spinodal in this analysis. The fundamental equation for nucleation near the spinodal is then

$$\frac{\partial\psi(\vec{x},t)}{\partial t} = -MR^d[-\nabla^2\psi(\vec{x},t) + \Delta h - C\psi^2(\vec{x},t)], \tag{5.8}$$

where we have set $C=12|\epsilon|^{1/2}/6^{1/2}$.

The nucleation or critical droplet is assumed to be an equilibrium fluctuation ([see [34,35,41–43]) and therefore should be a solution to the time-independent form of Eq. (5.8),

$$-\nabla^2\psi(\vec{x}) + \Delta h - C\psi^2(\vec{x}) = 0. \tag{5.9}$$

To understand how the droplet scales, we do not have to solve Eq. (5.9). We need only note that

$$\psi(\vec{x}) \sim (\Delta h)^{1/2}\overline{\psi}(\vec{x}(\Delta h)^{1/4}), \tag{5.10}$$

where $\overline{\psi}(\vec{x}(\Delta h)^{1/4})$ is of order 1 and a solution to

$$-\nabla^2\overline{\psi}(\vec{x}) + 1 - C\overline{\psi}^2(\vec{x}) = 0. \tag{5.11}$$

In order to see that this is indeed a critical droplet, we can specialize to one dimension ($d=1$) [37]. In one dimension, Eq. (5.9) reduces to

$$-\frac{d^2\psi(x)}{dx^2} + \Delta h - C\psi^2(x) = 0. \tag{5.12}$$

There are two boundary conditions required by the equation and those are fixed by physical considerations associated with the idea of an isolated droplet. First, as $x\to\infty$ we expect $\psi(x)$ to approach its value in the metastable state, $\psi_{\rm ms}$. This can easily be seen from Eq. (5.7), once all derivatives are set equal to zero, to be $\psi_{\rm ms}=-[\Delta h/C]^{1/2}$. The second boundary condition is that the droplet should be smooth so that we expect $d\psi(x)/dx=0$ at $x=0$. With these conditions, the solution of Eq. (5.12) is

$$\psi(x) = -\left(\frac{\Delta h}{C}\right)^{1/2} + 3\left(\frac{\Delta h}{C}\right)^{1/2}\frac{1}{\cosh^2\left(\dfrac{C^{1/4}\Delta h^{1/4}}{\sqrt{2}}x\right)}, \tag{5.13}$$

which has all of the scaling properties derived above.

We now test the stability of this solution to Eq. (5.12) by performing a linear stability analysis. We insert

$$\psi(x,t) = \psi(x) + \eta(x,t), \tag{5.14}$$

where $\psi(x)$ is given in Eq. (5.13), into

$$\frac{\partial\psi(x,t)}{\partial t} = -MR^d\left(-\frac{\partial^2\psi(x,t)}{\partial x^2} + \Delta h - C\psi^2(x,t)\right) \tag{5.15}$$

and linearize with respect to $\eta(x,t)$, which is assumed to be a small perturbation. We obtain

$$\frac{\partial\eta(x,t)}{\partial t} = -MR^d\left\{-\frac{\partial^2\eta(x,t)}{\partial x^2} + 2C\left[\left(\frac{\Delta h}{C}\right)^{1/2} - 3\left(\frac{\Delta h}{C}\right)^{1/2} \times \frac{1}{\cosh^2\left(\dfrac{C^{1/4}\Delta h^{1/4}}{\sqrt{2}}x\right)}\right]\eta(x,t)\right\}. \tag{5.16}$$

This equation has solutions of the form $\eta(x,t) = e^{-\lambda_i x}\eta_i(x)$, where the λ_i are the eigenvalues associated with the eigenvectors $\eta_i(x)$ of the operator

$$\lambda_i\eta_i(x) = -MR^d\left\{-\frac{d^2\eta_i(x)}{dx^2} + 2C\left[\left(\frac{\Delta h}{C}\right)^{1/2} - 3\left(\frac{\Delta h}{C}\right)^{1/2} \times \frac{1}{\cosh^2\left(\dfrac{C^{1/4}\Delta h^{1/4}}{\sqrt{2}}x\right)}\right]\eta_i(x)\right\}. \tag{5.17}$$

Equation (5.17) has the form of a time-independent Schrödinger equation with a shallow (since $\Delta h\ll 1$) well. One expects that there will be both positive and negative eigenvalues corresponding to bound and free states. This is indeed the case. One can show [34,37] that there is one negative eigenvalue and a continuum of positive eigenvalues. The eigenvector with negative eigenvalue, $\eta_o(x)$, is then unstable since its amplitude grows exponentially with time. One can easily see [34] that the eigenvector with negative eigenvalue has the form

$$\eta_o(x) \sim \frac{1}{\cosh^3\left(\dfrac{C^{1/4}\Delta h^{1/4}}{\sqrt{2}}x\right)}. \tag{5.18}$$

It is also easy to see that the negative eigenvalue $-\lambda_0$, where $\lambda_o>0$, scales as $\Delta h^{1/2}$. This implies that the droplet whose profile $\psi(x)$ is given in Eq. (5.13) is a saddle-point solution to Eq. (5.12) and that the system can move away from the metastable state via the growth of this saddle-point droplet. Moreover, the scaling of λ_o with $\Delta h^{1/2}$ implies that

the growth of the droplet slows as $\Delta h \to 0$. That is, the characteristic growth time t_g scales as $\Delta h^{-1/2}$. Before discussing the simulation test of this prediction, there are other quantities that we can predict from the theoretical treatment of the CA model which can also be tested via simulation. In order to obtain these predictions, it is necessary to go a bit deeper into nucleation theory.

As stated above, one of the main assumptions of nucleation theory is that the critical, or nucleating, droplet can be viewed as an equilibrium fluctuation [43]. This implies from Eqs. (5.1) and (5.7) that the probability of a critical droplet is proportional to the partition function evaluated at the saddle-point solution associated with the critical droplet [34,43]. The proportionality factor, or prefactor, comes in two parts [35,44]. The static part is given by the Gaussian integral associated with the steepest-descent part of the saddle-point evaluation of the partition function [34,35,43]. The form of the static part to the prefactor is $\xi^{-d} \sim R^{-d} \Delta h^{d/4}$.

The kinetic part of the prefactor depends on the form of the dynamics driving the system. In particular, it depends on the conservation laws and how conserved quantities couple to the variable $\psi(x)$. In the Langevin dynamics we are discussing in this section, as well as in the dynamics for the earthquake model, the kinetic prefactor scales as $\Delta h^{1/2}$ [34].

Combining these factors, we obtain the probability per unit time of a critical or nucleating droplet $P_n(\Delta h)$ to be

$$P_n(\Delta h) = \frac{A \Delta h^{1/2} \exp[-B \beta R^d \Delta h^{3/2-d/4}]}{\xi^d}. \quad (5.19)$$

The constants A and B are independent [37] of Δh and are not relevant to our discussion. The factor $\Delta h^{-1/2}$ sets the time scale. Since the droplets are assumed to be independent of each other, then $P_n(\Delta h)$ is proportional to the number of droplets per unit volume. From Eq. (5.19) it can be seen that for a fixed Δh, $P_n(\Delta h)$ is exponentially damped in R. In the mean-field limit, $R \to \infty$, nucleation is completely suppressed. However, for fixed R, which is more in line with simulations, the exponential part of $P_n(\Delta h)$, usually known as the nucleation barrier, can be made smaller by decreasing Δh. Due to the exponential dependence on Δh, the probability of a critical droplet remains quite small until the argument of the exponential becomes of order 2–3. This is usually referred to in the literature as the Becker-Döring limit or limit of metastability [40]. Nucleation will occur from the metastable state on some time scale no matter what the size of the nucleation barrier. For practical purposes, however, in simulations such as the ones we are performing, nucleation will occur only in the vicinity of the Becker-Döring limit where the time scales become attainable. For this discussion we do not need to know the precise value of this limit. We only need to note that the condition that nucleation occur only in the neighborhood of this limit implies that

$$R^d \Delta h^{-d/4} = \xi^d = D \Delta h^{-3/2}, \quad (5.20)$$

where D is a constant independent of Δh.

We are now in a position to derive one of the three scaling relations we have tested with simulations on the CA model. The first is a scaling relation between the mean equilibration time t_{equil} and K. The equilibration time is defined as the number of time steps required for the system to relax after a plate update. Taking the time average of each equilibration time over all plate updates determines the mean equilibration time, which is the mean time to form an earthquake. Our prediction is that this equilibration time will scale with the correlation length in analogy with the ''ϕ^4'' model. To obtain this scaling in variables appropriate to the CA model, we note that from Eqs. (3.6) and (3.7), K behaves as a field, similar to the external magnetic field in the ϕ^4 model discussed above. That is, varying K either brings the system closer to the spinodal (increasing K) or moves it further away. The location of the spinodal for $V \sim 0$ will be $K^{-1} \sim 0$. The correlation length, or mean radius of gyration, of the earthquake clusters will scale as

$$\xi \sim K^{1/4}, \quad (5.21)$$

in analogy to $\xi \sim \Delta h^{-1/4}$ in the ϕ^4 model. Direct comparison of Eq. (3.5) with Eq. (5.8) leads to the conclusion that the characteristic, or growth, time

$$t_g \sim \xi^2 \sim K^{1/2}. \quad (5.22)$$

This relation means that as K increases and brings the system closer to the spinodal, the mean time to form an earthquake increases, corresponding to critical slowing down as observed in condensed-matter systems near critical points. Figure 6 shows that for large $q = 1088$ (circles), but much smaller than the system size, t_g follows a power-law form of $t_g \sim K^{0.35 \pm 0.1}$. However, as the interaction region includes more blocks $q \approx 10\,000$ (diamonds), or becomes more mean field, the data points approach the predicted mean-field result given in Eq. (5.22).

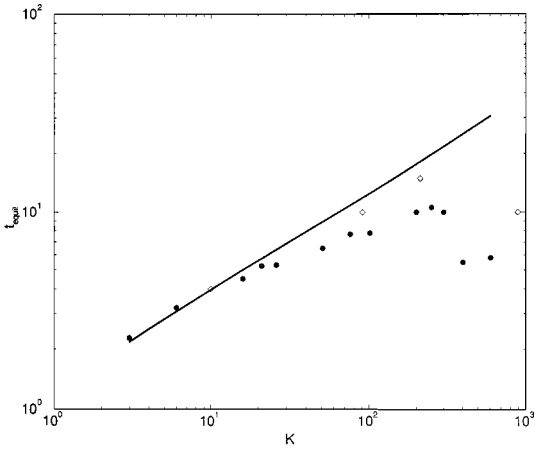

FIG. 6. Log-log plot of the mean equilibration time to form a cluster per plate update versus the effective spring constant K. The circles are for a 256×256 system with $V \sim 0$, $\sigma^F = 50$, $K_L = 1$, $W = 0.3$, and $q = 1088$ using the K_C/q interaction. The diamonds are for a 128×128 system with $V \sim 0$, $\sigma^F = 50 \pm 10$ (random uniform distribution of failure thresholds), $\sigma^R = 0$, $K_L = 1$, and $q \approx 10\,000$ using the $1/r^3$ truncated interaction. The straight line has a slope of $\frac{1}{2}$, the predicted mean-field exponent.

A very interesting and important aspect of these data which not only impacts on our understanding of this class of models, but also has implications for understanding spinodal nucleation in condensed-matter systems, is the large value of q required to see the critical slowing down predicted by the

mean-field theory. Large values of q allow the spinodal to be more closely approached by raising the nucleation barrier [see Eq. (5.19)] and hence decreasing the value of Δh needed to reach the Becker-Döring limit.

In order to derive the next two scaling relations, we need to introduce the idea of arrested nucleation. We begin by noting from Eq. (3.7) that the low velocity phase is a low stress phase. As the system is brought closer to the spinodal by raising the velocity or the coupling constant K, the low stress phase becomes metastable and the high stress phase becomes stable. One would expect then that nucleation would take the system from the low stress metastable phase into the high stress stable phase. However, the high stress phase is not seen in the simulations performed in this work. Our hypothesis is that the nucleation process is stopped, or arrested. We will discuss the mechanism responsible for stopping the nucleation events in Sec. VII. In this section we will pursue the consequences of this idea.

Our working hypothesis is that large stress saddle-point objects occur as in the theory outlined above. These objects are stopped or arrested and decay. The release of the stress from the high stress region during the decay is the earthquake. We have found these high stress regions in simulations, and those data will be presented in a future publication [29].

Since the earthquake is associated with the release of stress, the number of failed blocks should be proportional to the number of high stress blocks. That is, we are claiming that the high stress region defines the region of the earthquake in this model as it is presently simulated and that the Gutenberg-Richter scaling, as well as other scaling laws, can be obtained from understanding the statistical distribution of the high stress regions.

This raises the question as to why we believe that the only blocks that fail in the earthquake are those originally in the high stress region. First, that is essentially what the simulations show in this work and in other versions of the model we have studied [29]. The number of breakout events is a small fraction of the total number and that fraction decreases as we increase q. In addition, the time scale between breakout events and the time scale over which the fluctuation metric analysis indicates that the system is ergodic are of the same order [45].

Second, we have done an analysis of what conditions would favor such a containment and what would favor breakout from the high stress region resulting in a characteristic event in which approximately all blocks in the system fail [46]. That study indicated that the stress profile in the model, as it is run in these studies, is too rough for a significant number of breakout events to occur and that the statistics will be dominated by scaling events that are contained within the original high stress region. The stress profile is defined as the field $\sigma^F - \overline{\sigma}(\vec{x},t)$. By rough we mean a surface defined by the stress profile in $d=2$ with a fractal dimension greater than 2.5.

With these considerations the mean mass of the clusters $\overline{s}$ will scale as the mean mass of the nucleation or critical droplet. From Eqs. (5.10) and (5.13), the density of the critical droplet scales as $\Delta h^{1/2}$ and its volume as ξ^d. This implies that the mass of the critical droplet $\overline{s}$ scales as

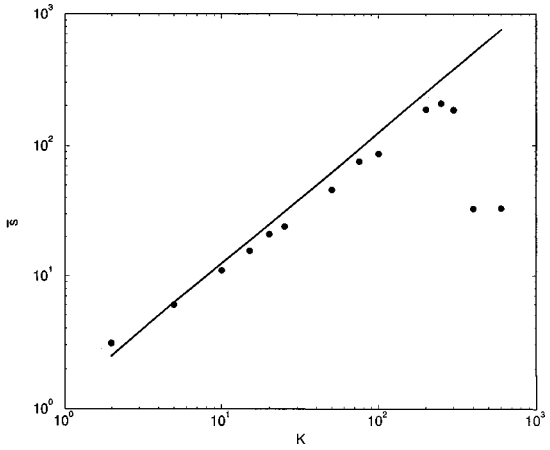

FIG. 7. Log-log plot of the mean cluster size $\overline{s}$ versus the effective spring constant K. The 256×256 system has $V\sim0$, $\sigma^F=50$, $K_L=1$, $W=0.3$, and $q=1088$ using the K_C/q interaction. The straight line has a slope of 1, the predicted mean-field exponent.

$$\overline{s}\sim\xi^d\Delta h^{1/2}. \tag{5.23}$$

From the condition that nucleation take place near the Becker-Döring limit and Eq. (5.20), we have

$$\overline{s}\sim\Delta h^{-1}. \tag{5.24}$$

As in the above discussion, we can express this relation in terms of K. That is, $K\sim\Delta h^{-1}$ so that $\overline{s}\sim K$. The data in Fig. 7 are clearly consistent with this prediction.

Finally, in this section we derive the exponent for cluster scaling. Since critical slowing down is only cleanly attainable for extremely large q, we will remove it from the calculation of nucleation rates by measuring the number of clusters of size s, $n_c(s)$, normalized by the total number of clusters. This takes the time element out of the calculation. We expect then that the number of critical droplets over a time scale proportional to $\Delta h^{-1/2}$ is proportional to ξ^{-d}, where we have used Eq. (5.19) multiplied by the time (proportional to $\Delta h^{-1/2}$) and assumed, as usual, that $R^d\Delta h^{3/2-d/4}$ is a constant since nucleation takes place only near the Becker-Döring limit. From our assumption that the mass of the earthquakes scales like the critical droplet, we have that the number of earthquakes or clusters per unit volume scales as ξ^d. But ξ^d is related to $\overline{s}$ through

$$\overline{s}\sim\xi^{2d/3}. \tag{5.25}$$

This follows from Eqs. (5.20) and (5.23). Clearly this implies from the above discussion and Eq. (5.19) that

$$n_c(s)\sim\frac{1}{s^{3/2}}. \tag{5.26}$$

Figures 8 and 9 demonstrate that the simulations confirm this analytic result. Note that even with the two different forms of the long-range interaction, as shown in Figs. 8 and 9, the model produces the same mean-field exponent.

This scaling exponent for clusters, together with assumptions of how the slip scales with the number of failed blocks, translates into a Gutenburg-Richter b value of $\frac{3}{4}$. If critical slowing down is included in the nucleation rate, the same

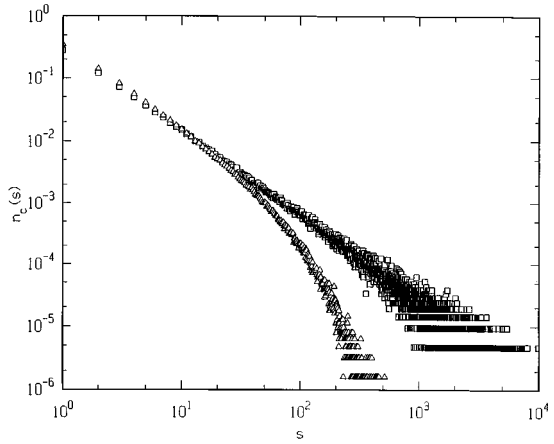

FIG. 8. Log-log plot of the number of clusters $n_c(s)$ with s failed blocks divided by the total number of clusters. The 128×128 system was run with $V\sim0$, $\sigma^F=50$, $\sigma^R=0$, and $K_L=1$, using the truncated $1/r^3$ interaction. The triangles are for $K=9.95$ and the squares correspond to $K=90.45$. The slope of the straight part of the curves is 1.5 ± 0.1 for the triangles and 1.38 ± 0.15 for the squares. Both slopes are consistent with $\frac{3}{2}$ as predicted by the theory.

arguments used above give a cluster scaling exponent of 2 and a b value of 1. The reader interested in the details is referred to Ref. [47].

As we mentioned above, the arrested nucleation droplets are associated with the large events. The smaller events we associated with the critical phenomena fluctuations near the spinodal. Since the clusters associated with the spinodal critical point have the same scaling as the arrested nucleation droplets without critical slowing down [48,49], we would expect the same scaling for both regions of the cluster scaling curves in Figs. 8 and 9. There should be a relative displacement in the straight lines but the normalization with the total number of clusters makes this displacement impossible to see.

The scaling curve for the mean cluster size versus K will

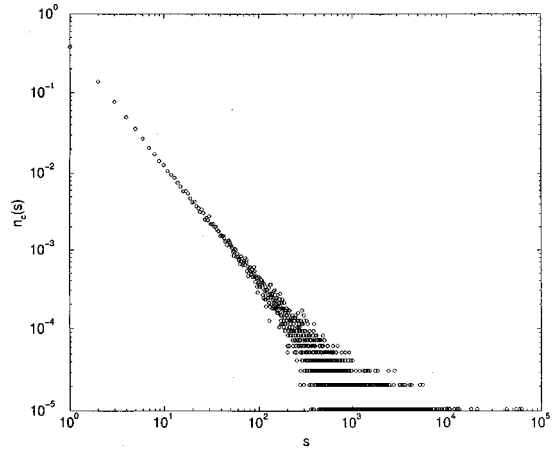

FIG. 9. Log-log plot of the number of clusters $n_c(s)$ with s failed blocks divided by the total number of clusters. The 256×256 system was run with $V\sim0$, $\sigma^F=50$, $W=0.3$, $K_L=1$, $K_C=50$, and $q=1088$ using the K_C/q interaction. The slope of the straight part of the curve is 1.5 ± 0.1, which is consistent with the theory's prediction of $\frac{3}{2}$.

not be affected by the fact that the smaller clusters associated with the critical phenomena fluctuations scale differently than arrested nucleation droplets since the mean cluster size is dominated by the much larger clusters associated with arrested spinodal nucleation. The approximate size of these two types of objects is estimated below.

Finally we point out that, while critical phenomena fluctuations can explain the smaller cluster end of the cluster scaling curves in Figs. 8 and 9, they cannot explain the upper end of theses scaling plots. Conversely, arrested nucleation droplets have the right scale for the larger end of the cluster scaling but not the lower end.

To see this, we return first to the mean size $\overline{s}$ of the arrested nucleation droplets given in Eq. (5.23), i.e.,

$$\overline{s}=\xi^d\Delta h^{1/2}. \tag{5.27}$$

Since $\xi^d\Delta h^{1/2}=q\Delta h^{-1/2}$ in $d=2$, we have that the arrested nucleation droplets have a mean size $\overline{s}\sim10^3$. Clearly this is only an estimate, but $\overline{s}$ is consistent with the upper end of the scaling plot in Fig. 9. We expect some spread in the size of the arrested nucleation droplets, but if the mean size is of order 10^3 it is difficult to imagine nucleation or activation events at a scale of order 10, which is the lower end of the scaling plots in Figs. 8 and 9.

The solution to this problem we believe is to consider another mechanism for events at the smaller mass scales. Since we are near a mean-field spinodal, or more precisely a pseudospinodal, we should expect critical phenomena fluctuations as well as arrested nucleation droplets. This is in analogy with the standard ''ϕ^4'' models [34]. We can estimate the size of the clusters associated with the critical phenomena fluctuations by first noting that the distance from the spinodal of the simulations that gave rise to the scaling plots in Figs. 8 and 9 is of order 10^{-2}. We can see that first by noting that if K^{-1} is used as a scaling field as it is in Fig. 8, the straightest line is for $K\sim10^2$. In Fig. 9, where a slightly different form of the potential is used, the value of K is 0.5×10^{-2}. Note that Eq. (3.8) implies that for $V\sim0$ the spinodal value of $K^{-1}\sim0$.

For critcal phenomena clusters near spinodals, the mass or mean size scales as

$$\overline{s}\sim\frac{\Delta h^{1/2}}{R^d\Delta h^{3/2-d/4}}R^d\Delta h^{-d/4}. \tag{5.28}$$

The derivation and details of this scaling can be found in Refs. [25] and [50]. With $\Delta h\sim10^{-2}$ and $d=2$ we have that the size of the clusters associated with critical phenomena fluctuations is on the order of 100. Note that the mean cluster size is an average over all clusters and hence is dominated by the larger clusters in the scaling plot. The mean size of 100 gives us an estimate of the region of the upper end of the cluster scaling associated with the critical phenomena clusters. Larger clusters would be in the exponential decay. This indicates, as stated earlier, that associating the larger end of the scaling plot for the ''earthquakes'' with critical phenomena fluctuations is untenable.

As a footnote to this section, we want to point out that the derivation of these scaling laws implicitly makes use of the fact that there is only one divergent length in the system that

controls all singular behavior. This is the so-called hyperscaling assumption. In general, mean-field systems do not have hyperscaling except in the upper critical dimension, which in this case is 6 [37]. However, the condition that nucleation take place only in the vicinity of the Becker-Döring limit fixes $R^d \Delta h^{3/2-d/4}$ and restores hyperscaling. The discussion of this point is subtle. The interested reader can find the details in [50].

VI. ENERGY-FLUCTUATION METRIC AND ERGODICITY

We have been applying equilibrium statistical mechanics to the CA model. Before we can use these methods, we must establish that this model displays the characteristics of an equilibrium system under the conditions we have used in the simulations. Recently, Rundle *et al.* [14] demonstrated that the CA model exhibits Boltzmann fluctuations in its internal energy field for $K \gg 1$, i.e., near mean field. In this section, we present evidence that this model tends toward an ergodic system as the interactions become long-range by using a numerical test, called the energy-fluctuation metric $\Omega(t)$ [15], which determines if a simulated system is effectively ergodic over an observational time scale. The quantity $\Omega(t)$ measures the difference between the time average and the ensemble average of a system's energy and is defined as

$$\Omega(t) = \frac{1}{N} \sum_{i=1}^{N} [\epsilon_i(t) - \overline{\epsilon}(t)]^2, \tag{6.1}$$

where the sum runs over the N blocks of the system, the running time average of block i's energy $\epsilon_i(t)$ from $t' = 0$ to t is

$$\epsilon_i(t) = \frac{1}{t} \int_0^t \epsilon_i(t')\, dt', \tag{6.2}$$

and the spatial average of the energy is

$$\overline{\epsilon}(t) = \frac{1}{N} \sum_{i=1}^{N} \epsilon_i(t). \tag{6.3}$$

For ergodic systems, $\Omega(t) \sim 1/t$ [15]. Consequently, plots of $1/\Omega(t)$ versus t increase linearly if a system is effectively ergodic.

We will illustrate the effects of the loader plate velocity V, interaction range R, and spring constant K_C on the energy-fluctuation metric $1/\Omega$. Figure 10 shows $1/\Omega$ versus loader plate update n for constant R as V increases from 0.01 to 1 from top left to bottom right. Each plot uses the same abscissa scale for ease of comparison. The top two plots do not depict the initial transient due to the initial conditions. As V decreases, $1/\Omega$ becomes straighter and increases in a more linear fashion over a longer time.

Figure 11 shows $1/\Omega$ versus n for varying R. As in Fig. 10, each plot uses the same abscissa scale and does not depict the initial transient. Comparing the top right and bottom two plots, observe that as the interaction range increases from nearest neighbors to $R = 4$, $1/\Omega$ becomes straighter and increasingly linear over a longer time. Note that in these plots, we are moving the loader plate at what we call a ''critical'' velocity V_c, in which frequency-size plots produce power-law scaling over a narrow range of velocities centered about V_c. We emphasize that this scaling results from the coalescence of typically many initial growth sites during each plate update. While we recognize that this coalescence violates the separation of time scales inherent in most earthquake processes, we have driven the system in this manner in order to have a reference velocity V_c that gives similar ''critical'' behavior for different interaction ranges. This allows us to examine the ergodicity differences for different interaction ranges, R. The top left and bottom right plots in Fig. 11 show that for a constant V but different R, $1/\Omega$ shows a more linear increase over a longer time as R goes from nearest neighbors to $R = 4$.

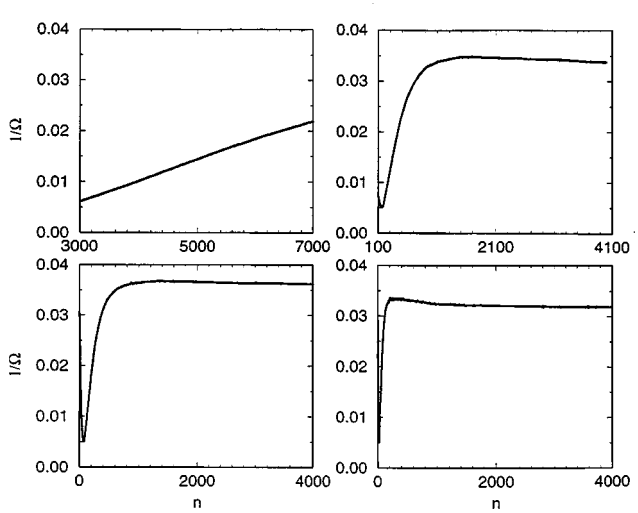

FIG. 10. Inverse of the energy-fluctuation metric $1/\Omega$ versus loader plate update n for a 256×256 lattice with closed boundaries and $R = 4$ ($q = 80$), using parameters $\sigma^F = 50 \pm 10$ (random uniform distribution of failure thresholds), $\sigma^R = 0$, and $K_C = K_L = 1$. From left to right and top to bottom, $V = 0.01$, 0.15, 0.3086, and 1.

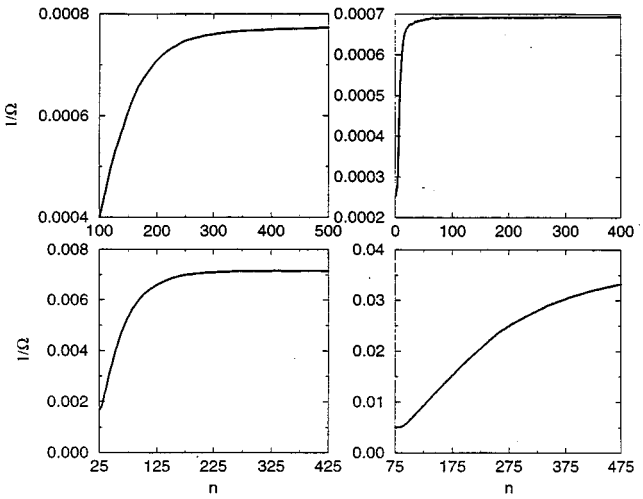

FIG. 11. Inverse of the energy-fluctuation metric $1/\Omega$ versus loader plate update n using the same parameters as Fig. 10, except for R and V. From left to right and top to bottom, R = nearest neighbors and $V = 0.3086$; R = nearest neighbors and $V = V_c = 5.0$; $R = 2$ ($q = 24$) and $V = V_c = 1.0$; and $R = 4$ ($q = 80$) and $V = V_c = 0.3086$.

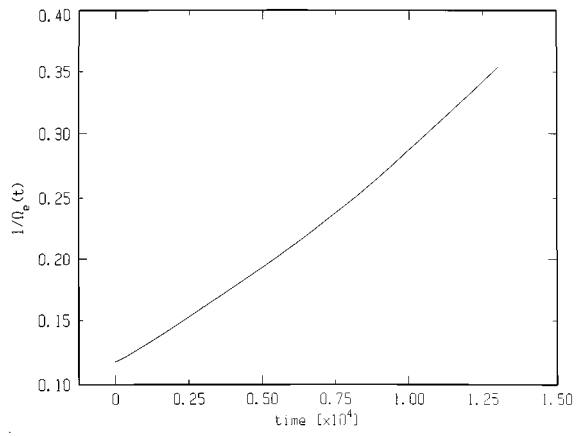

FIG. 12. Inverse of the energy fluctuation metric $1/\Omega$ versus loader plate update n for a 256×256 lattice with closed boundaries and $R=4$ ($q=80$), using parameters $\sigma^F=50$, $K_L=1$, $K_C=100$, $V=0.001$, and $W=0.1$.

In comparison to Fig. 11, using realistic fault parameters of $V=0.001$, which produces about one initial growth site per plate update, and of $K_C=100$ and $K_L=1$, which correspond to strong coupling among the blocks and relatively weak coupling to the loader plate, Fig. 12 shows that $1/\Omega$ displays linear behavior over a long time. If we remove the coupling among the blocks by setting $K_C=0$, the system does not exhibit ergodic behavior, as shown in Fig. 13. Here the sinusoidal character of $1/\Omega$ [16] arises from the quasiperiodic movement of the blocks as the loader plate continually drives them to σ^F and they relax to σ^R. The energy-fluctuation results indicate that as $V\rightarrow0$ and as R and K_C increase, the CA system becomes more ergodic. This observation, in conjunction with the previous findings demonstrating Boltzmann statistical fluctuations [14], indicates that the long-range, slowly driven CA system tends toward an equilibrium system.

Our interpretation of this result is that the free-energy surface obtained by functionally integrating Eq. (3.6) has multiple minima within the low stress phase. These minima correspond to different energies. Small events, which are contained within the high stress region, as discussed in the preceding section, appear to leave the system in the same free-energy minimum. Breakout events, which are relatively rare in our simulations and become less frequent as q is increased, seem to push the system into a new minimum. This interpretation, and its confirmation, is the subject of current investigation.

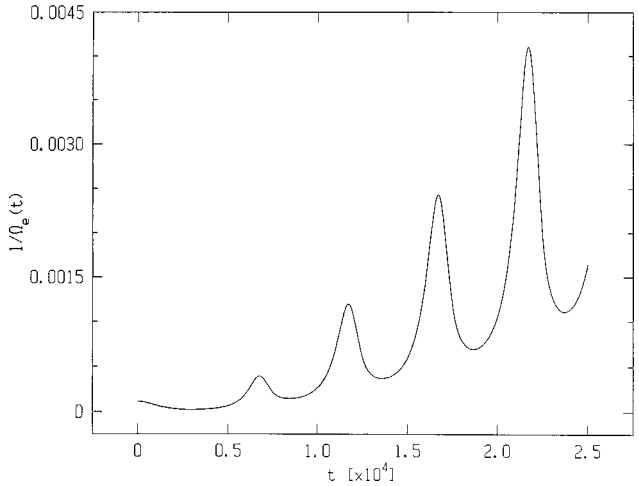

FIG. 13. Inverse of the energy-fluctuation metric $1/\Omega$ versus loader plate update n using the same parameters as Fig. 12, except $K_C=0$.

VII. COARSE GRAINING REVISITED AND ARRESTED NUCLEATION

In this section we return to the discussion of arrested nucleation. The question we need to address is what causes the nucleation of the high stress phase to be halted so that it is never seen in these simulations. The answer to this question requires that we reexamine the coarse-graining procedure and the derivation of Eq. (3.6).

As discussed in Sec. IV, there is a coarse-graining time which is the fundamental time unit in our coarse-grained description. That is, the fundamental time unit in Eq. (3.6) is the time scale required to have the stress distribution in a coarse-grained volume become Gaussian. This will, as seen in Sec. IV, require a finite fraction of the number of blocks in the coarse-grained volume to fail. This time is not constant, however, in units of plate update time. Since the coarse-graining time is the basic unit of time that we are forced to have once we adopt a coarse-grained description, this implies that the unit of plate update time and, hence, the plate velocity is not constant but is in fact a fluctuating variable.

Clearly, the plate update number required to fail a finite but fixed number of blocks depends on the size of the ''earthquake'' events that occurs as that fraction of blocks fails. The larger the events, the smaller the number of plate updates, and, hence, the slower the velocity of the plate in units of coarse-graining time. This implies that the coarse-grained loading rate depends on the ''earthquake'' activity during the coarse-grained time unit. We expect then that the velocity of stress loading, or the plate velocity, will be lowered by increased ''earthquake'' activity and increased by decreased activity. In the mean-field model, all sites fail at the failure threshold as discussed in Sec. IV. This allows us to relate the number of failures in an event to the stress change. With these considerations we can express the time-dependent velocity $V(\tau)$ as

$$V(\tau)=V+\frac{\alpha}{L^2}\int d\vec{x}\frac{\partial\sigma_D(\vec{x},\tau)}{\partial\tau}, \tag{7.1}$$

where L^2 is the volume of the system in $d=2$, α is a positive constant, and the time derivative of $\sigma_D(\vec{x},\tau)$ is the rate at which stress is dissipated at $\vec{x}$ at time τ. Note that for static considerations the time derivative vanishes and we return to the situation discussed in Sec. IV and Eq. (3.7). However, when we are considering time-dependent quantities, the $\int d\vec{x}[\partial\sigma_D(\vec{x},\tau)/\partial\tau]$ term in the plate velocity will now depend on τ. Also note that when the net rate of stress dissipation is negative, as would occur during times of large earthquake activity, the time-dependent velocity $V(\tau)$ is lower than the bare velocity V, which is now the time average, over infinite time, of $V(\tau)$ in a steady state. The idea of arrested nucleation is that large events are preceded by an

increased activity in this model and this activity drives the plate velocity down, effectively raising the nucleation barrier.

There are three points that need to be made about this velocity modification. The first is that we can relate the time dependence of the velocity to the rate of stress dissipation only in the mean-field limit where all blocks fail at the failure threshold as discussed in Sec. IV. Second, the term

$$\frac{\partial \sigma_D(\vec{x},\tau)}{\partial \tau} \propto \sqrt{\beta/\pi}\int_{\sigma_0}^{\sigma^F} d\sigma \exp\{-\beta[\sigma-\overline{\sigma}(\vec{x},\tau)]^2\}, \tag{7.2}$$

as can be seen from Eqs. (3.4) and (3.6). Finally these considerations predict that there should be increased activity before any large events that could be described as arrested nucleation, where ''before'' refers to the coarse-graining time interval preceding the arrested nucleation event. This has been seen to be correct. The data and a detailed discussion will be presented in a future publication [29]. We have also tested this idea by performing simulations [29] in which the plate updates were done so that the amount of stress put into the system was proportional to the number of blocks that failed after the preceding plate update. In the mean-field limit, this insures that the plate velocity is a constant in units of the coarse-graining time. With this form of update, the high stress phase was observed [29], consistent with the ideas presented in this section.

VIII. SUMMARY AND CONCLUSION

In this paper we have presented theoretical arguments and data that support our assertion made in a previous publication [13] that slider-block models of the type described in Refs. [4] and [5] obey an Ito-Langevin equation in the limit of long-range stress transfer. This derivation and the energy-fluctuation metric studies in Sec. VI also support our conclusion, based on data analysis [14], that the slider-block system can be described with equilibrium techniques in the mean-field limit. Also see Refs. [51] and [52] for additional discussion of this point.

The energy-fluctuation metric study in Sec. VI also shows that the time scale over which the slider-block system can be described with equilibrium techniques for systems with finite-range stress transfer is finite and grows longer as the range of the stress transfer increases.

The picture that emerges from these considerations is of a multiple minima, high dimensional, free-energy surface (in the system with noise) where the system remains trapped in a particular well for a time scale that diverges as the stress transfer range goes to infinity, that is, in the mean-field limit.

Another result that emerges from this work is the association of GR scaling with a spinodal, or pseudospinodal. We have argued that the lower or smaller end of the cluster scaling plots in Figs. 8 and 9 can be explained by associating ''earthquake'' events with critical phenomena fluctuations. However, the upper or larger end of the scaling plots have clusters that are too large to be explained by critical phenomena scaling at the distance the data were taken from the spinodal critical point. We have explained these larger events with the concept of arrested nucleation and provided a theoretical derivation of cluster number scaling, critical slowing down, and cluster-size scaling that are consistent with data from simulations of the model. We have also discussed the mechanism that we believe is responsible for the arresting of the nucleation, namely that the plate velocity is not constant in the right time frame but must be treated as a fluctuating variable. We have also mentioned the results of two additional tests that support this idea [29]. This work, together with the study in Ref. [46], indicates that in this model there are at least three separate ''earthquake'' orders of magnitude that are generated by different mechanisms. The smallest is associated with critical phenomena fluctuations near the spinodal critical point. The second largest is associated with arrested spinodal nucleation and the third, which is not on the scaling plot (i.e., these events do not scale on a single fault), is associated with breakout events.

Finally, these results raise several interesting questions. Among them are the relation between the events of different sizes that we have seen and the different size events seen in the work of Carlson, Langer, and Shaw [6], the possible existence of additional event size scales, the possible connection between breakout events and the breaking of ergodicity in the energy-fluctuation metric, and the relation between the events on the various size scales. For example, can critical phenomena size events trigger a breakout event or can that only be done by an arrested nucleation event? These and other questions raised by this work are currently being pursued.

ACKNOWLEDGMENTS

C.D.F. and W.K. received support from U.S. DOE Grant No. DE-FG02-95ER14498, and J.B.R. received support from U.S. DOE Grant No. DE-FG03-95ER14499. We acknowledge useful conversations with F. Alexander, R. Brower, H. Gould, and J. Goldstein. We also acknowledge assistance from the Center for Information Technology of Boston University.

[1] B. Gutenberg and C. F. Richter, *Seismicity of the Earth and Associated Phenomena* (Princeton University Press, Princeton, 1954).

[2] J. C. Gu, J. R. Rice, A. L. Ruina, and S. T. Tse, J. Mech. Phys. Solids **32**, 167 (1984).

[3] J. Huang and D. Turcotte, Nature (London) **348**, 234 (1990).

[4] J. B. Rundle and D. D. Jackson, Bull. Seismol. Soc. Am. **67**, 1363 (1977).

[5] J. B. Rundle and S. R. Brown, J. Stat. Phys. **65**, 403 (1991).

[6] J. M. Carlson and J. S. Langer, Phys. Rev. A **40**, 6470 (1989); **44**, 884 (1991); J. M. Carlson, J. S. Langer, and B. E. Shaw, Rev. Mod. Phys. **66**, 657 (1994).

[7] P. Bak and C. Tang, J. Geophys. Res. **94**, 15635 (1989).
[8] H. J. S. Feder and J. Feder, Phys. Rev. Lett. **66**, 2669 (1991).
[9] Z. Olami, H. J. S. Feder, and K. Christensen, Phys. Rev. Lett. **68**, 1244 (1992).
[10] J. B. Rundle and W. Klein, J. Stat. Phys. **72**, 405 (1993).
[11] R. Burridge and L. Knopoff, Bull. Seismol. Soc. Am. **57**, 341 (1967).
[12] G. L. Vasconcelos, Phys. Rev. Lett. **76**, 4865 (1996).
[13] W. Klein, J. B. Rundle, and C. D. Ferguson, Phys. Rev. Lett. **78**, 3793 (1997).
[14] J. B. Rundle, W. Klein, S. Gross, and D. Turcotte, Phys. Rev. Lett. **75**, 1658 (1995).
[15] D. Thirumalai and R. D. Mountain, Phys. Rev. A **42**, 4574 (1990).
[16] D. Thirumalai and R. D. Mountain, Phys. Rev. E **47**, 479 (1993).
[17] M. de Sousa Vieira and H. J. Herrmann, Phys. Rev. E **49**, 4534 (1994).
[18] K. Rybicki, in *Continuum Theories in Solid Earth Physics*, edited by R. Teisseyre (Elsevier, Amsterdam, 1986).
[19] J. A. Steketee, Can. J. Phys. **36**, 192 (1958).
[20] J. B. Rundle and W. Klein, Nonlinear Proc. Geophys. **2**, 61 (1995).
[21] D. P. Hill *et al.*, Nature (London) **260**, 1617 (1993).
[22] J. Gomberg (unpublished).
[23] C. H. Scholz, *The Mechanics of Earthquakes and Faulting* (Cambridge University Press, Cambridge, 1990).
[24] J. B. Rundle, W. Klein, and S. Gross, in *Reduction and Predictability of Natural Disasters*, Santa Fe Institute Studies in the Sciences of Complexity Vol. XXV, edited by J. B. Rundle, D. L. Turcotte, and W. Klein (Addison-Wesley, Reading, MA, 1996).
[25] L. Monette and W. Klein, Phys. Rev. Lett. **63**, 2336 (1992).
[26] J. B. Rundle and W. Klein, Phys. Rev. Lett. **63**, 171 (1989).
[27] N. Gross, W. Klein, and K. Ludwig, Phys. Rev. Lett. **73**, 2639 (1994).
[28] For a description of the coarse-graining process, see S-K. Ma, *Modern Theory of Critical Phenomena* (Benjamin, Reading, MA, 1976).
[29] J. Goldstein, W. Klein, H. Gould, and J. Rundle (unpublished).
[30] Because the noise determines the parameter β, it sets the scale for the width of the Gaussian as well as the weight given to the ''entropy'' term. Although we use only one β for these two functions, using different β's would not substantially alter our conclusions.
[31] G. Nicolis and I. Prigogine, *Self Organization in Non-Equilibrium Systems* (Wiley, New York, 1977).
[32] W. H. Press, S. A. Teukolsky, W. T. Vetterling, and B. P. Flannery, *Numerical Recipes: The Art of Scientific Computing*, 2nd ed. (Cambridge University Press, Cambridge, 1992).
[33] D. W. Heermann, W. Klein, and D. Stauffer, Phys. Rev. Lett. **49**, 1262 (1982).
[34] C. Unger and W. Klein, Phys. Rev. B **29**, 2968 (1984).
[35] J. D. Gunton, P. Sahni, and M. San Miguel, in *Phase Transitions and Critical Phenomena, Vol. 8*, edited by C. Domb and J. Lebowitz (Academic, New York, 1983).
[36] J. Lee, M. A. Novotny, and P. A. Rikvold, Phys. Rev. E **52**, 356 (1995).
[37] W. Klein and C. Unger, Phys. Rev. B **28**, 445 (1983).
[38] T. Ray and W. Klein, J. Stat. Phys. **61**, 891 (1990).
[39] D. W. Heermann and W. Klein, Phys. Rev. Lett. **50**, 1062 (1983).
[40] D. W. Heermann and W. Klein, Phys. Rev. B **27**, 1732 (1983).
[41] J. W. Cahn and J. E. Hilliard, J. Chem. Phys. **28**, 258 (1958).
[42] J. W. Cahn and J. E. Hilliard, J. Chem. Phys. **31**, 688 (1959).
[43] J. S. Langer, Ann. Phys. (N.Y.) **41**, 108 (1967).
[44] J. S. Langer, Ann. Phys. (N.Y.) **54**, 258 (1969).
[45] C. D. Ferguson, Ph.D. thesis, Boston University (1996).
[46] J. B. Rundle, E. Preston, S. McGinnis, and W. Klein, Phys. Rev. Lett. **80**, 5698 (1998).
[47] J. B. Rundle, W. Klein, S. Gross, and C. D. Ferguson, Phys. Rev. E **56**, 293 (1997).
[48] W. Klein, Phys. Rev. Lett. **65**, 1462 (1990).
[49] D. Stauffer and A. Aharony, *Introduction to Percolation Theory* (Taylor and Francis, Washington, D.C., 1992).
[50] T. Ray and W. Klein, J. Stat. Phys. **53**, 773 (1988).
[51] H. J. Xu and D. Sornette, Phys. Rev. Lett. **78**, 3797 (1997).
[52] J. B. Rundle, W. Klein, S. Gross, and D. L. Turcotte, Phys. Rev. Lett. **78**, 3798 (1997).